

REPORT

XMAP215 promotes microtubule catastrophe by disrupting the growing microtubule end

Veronica Farmer^{1*}, Göker Arpağ^{1*}, Sarah L. Hall¹, and Marija Zanic^{1,2,3}

The GTP-tubulin cap is widely accepted to protect microtubules against catastrophe. The GTP-cap size is thought to increase with the microtubule growth rate, presumably endowing fast-growing microtubules with enhanced stability. It is unknown what GTP-cap properties permit frequent microtubule catastrophe despite fast growth. Here, we investigate microtubules growing in the presence and absence of the polymerase XMAP215. Using EB1 as a GTP-cap marker, we find that GTP-cap size increases regardless of whether growth acceleration is achieved by increasing tubulin concentration or by XMAP215. Despite increased mean GTP-cap size, microtubules grown with XMAP215 display increased catastrophe frequency, in contrast to microtubules grown with more tubulin, for which catastrophe is abolished. However, microtubules polymerized with XMAP215 have large fluctuations in growth rate; display tapered and curled ends; and undergo catastrophe at faster growth rates and with higher EB1 end-localization. Our results suggest that structural perturbations induced by XMAP215 override the protective effects of the GTP-cap, ultimately driving microtubule catastrophe.

Introduction

Microtubules are cytoskeletal polymers essential for cell motility, division, and intracellular transport. Microtubules are highly dynamic, allowing dramatic remodeling of the microtubule network to form cellular structures such as the mitotic spindle. Individual microtubule dynamics are characterized by “dynamic instability”: stochastic switching between phases of growth and shrinkage through transitions known as catastrophe and rescue (Mitchison and Kirschner, 1984). The standard model of dynamic instability implies that the presence of a stabilizing GTP-cap protects a growing microtubule against catastrophe. Namely, microtubules polymerize by incorporation of GTP-bound $\alpha\beta$ -tubulin heterodimers, followed by GTP hydrolysis in the β -tubulin subunits. The lag between GTP-tubulin addition and GTP hydrolysis results in a cap of GTP-tubulin dimers at the growing microtubule end. GTP hydrolysis triggers conformational changes that destabilize the GDP-tubulin lattice; loss of the GTP-cap exposes the unstable GDP lattice, thus triggering catastrophe (Mitchison and Kirschner, 1984; Desai and Mitchison, 1997).

The inability to directly visualize the GTP-cap has made its investigation challenging. Previous studies found that even a small cap, consisting of just a few GTP-tubulin layers, can be sufficient to stabilize a growing microtubule end (Drechsel and Kirschner, 1994; Strothman et al., 2019). Furthermore, an

increase in the GTP-cap size, which may occur due to an increase in growth rate, is typically associated with prolonged lifetime. Along those lines, early work demonstrated that increasing the microtubule growth rate by increasing the tubulin concentration in vitro is accompanied by a decrease in the catastrophe frequency (Walker et al., 1988). Although the exact functional dependence and the extent of catastrophe suppression have varied in subsequent reports, the finding that increase in tubulin concentration correlates with a decrease in catastrophe frequency remains generally supported (O'Brien et al., 1990; Drechsel et al., 1992; Odde et al., 1995; Gardner et al., 2011b; Bowne-Anderson et al., 2013; Piedra et al., 2016; Chaaban et al., 2018; Strothman et al., 2019; Arpağ et al., 2020). In recent years, microtubule-associated end-binding EB proteins, which display comet-like localization at growing microtubule ends (Bieling et al., 2007), have been established as markers for the GTP-cap due to their recognition of the nucleotide state of tubulin in the polymer (Zanic et al., 2009; Maurer et al., 2012; Zhang et al., 2015). In vitro studies investigating EB localization have revealed that increasing microtubule growth rate by increasing tubulin concentration correlates with larger EB comets (Bieling et al., 2007; Strothman et al., 2019). Additionally, microtubules with larger EB comets were more stable against catastrophe induced by tubulin dilution (Duellberg et al., 2016), providing

¹Department of Cell and Developmental Biology, Vanderbilt University, Nashville, TN; ²Department of Chemical and Biomolecular Engineering, Vanderbilt University, Nashville, TN; ³Department of Biochemistry, Vanderbilt University, Nashville, TN.

*V. Farmer and G. Arpağ contributed equally to this paper; Correspondence to Marija Zanic: marija.zanic@vanderbilt.edu.

© 2021 Farmer et al. This article is distributed under the terms of an Attribution-Noncommercial-Share Alike-No Mirror Sites license for the first six months after the publication date (see <http://www.rupress.org/terms/>). After six months it is available under a Creative Commons License (Attribution-Noncommercial-Share Alike 4.0 International license, as described at <https://creativecommons.org/licenses/by-nc-sa/4.0/>).

further evidence that suppression of catastrophe at faster growth rates may be a consequence of a larger GTP-cap.

In contrast to microtubules polymerized with purified tubulin *in vitro*, microtubules in cells can simultaneously display fast growth rates and high catastrophe frequency (Rusan et al., 2001; Mimori-Kiyosue et al., 2005; Akhmanova and Steinmetz, 2008; Akhmanova and Steinmetz, 2015). In cells, microtubule dynamics are tightly regulated by a myriad of microtubule-associated proteins (MAPs). Fast microtubule growth rates can be attributed to the action of microtubule polymerases, the most prominent belonging to the conserved XMAP215 family (Gard and Kirschner, 1987; Brouhard et al., 2008; Gard et al., 2004; Slep, 2009; Al-Bassam and Chang, 2011). On its own, XMAP215 increases growth rates up to 10-fold (Vasquez et al., 1994; Brouhard et al., 2008), while a combination of XMAP215 and EB1 synergistically promotes up to a 30-fold increase in growth rates, matching the fast rates observed in cells (Zanic et al., 2013). Surprisingly, although increasing growth rates by tubulin alone *in vitro* is accompanied by low catastrophe frequency, the significant increase in growth rate with XMAP215 was not accompanied by a suppression of catastrophe (Vasquez et al., 1994; Zanic et al., 2013). Importantly, the effect of XMAP215 on the size of the GTP-cap is not known.

Here, we investigate how XMAP215-promoted microtubule growth can simultaneously be fast and highly dynamic, displaying frequent microtubule catastrophes. First, we directly show that increasing tubulin concentration in the presence of EB1 increases growth rate and EB1 comet size, while simultaneously suppressing catastrophe frequency. Next, we add XMAP215 and demonstrate that XMAP215-driven increase

in microtubule growth rate is accompanied by both an increase in catastrophe frequency and an increase in EB1 comet size. Thus, the XMAP215-driven increase in catastrophe frequency is not a consequence of GTP-cap size reduction. Rather, we demonstrate that XMAP215 increases growth fluctuations and induces tapered and curled microtubule ends. Our results suggest that XMAP215-induced destabilization of the growing microtubule end ultimately promotes catastrophe.

Results and discussion

Increasing the microtubule growth rate by increasing tubulin concentration correlates with an increase in GTP-cap size and suppression of microtubule catastrophe

To directly investigate the relationship between microtubule growth rate, catastrophe frequency, and GTP-cap size, we used an established *in vitro* assay (Gell et al., 2010). Dynamic microtubule extensions were polymerized from GMPCPP-stabilized seeds using a range of tubulin concentrations (12–60 μM) and imaged with total internal reflection fluorescence (TIRF) microscopy (Fig. S1 A). To determine the size of the GTP-cap, we included 200 nM EB1-GFP in all conditions and measured the EB1 comet size at growing microtubule ends over a range of growth rates. The increase in growth rate achieved with tubulin titration was accompanied by a simultaneous suppression of catastrophe frequency (Fig. S1 B), consistent with studies using tubulin alone (Walker et al., 1988). In addition, increasing growth rates resulted in a linear increase in the average EB1 comet size (Fig. S1 C), consistent with previous reports (Bieling et al., 2007). Thus, our measurements directly

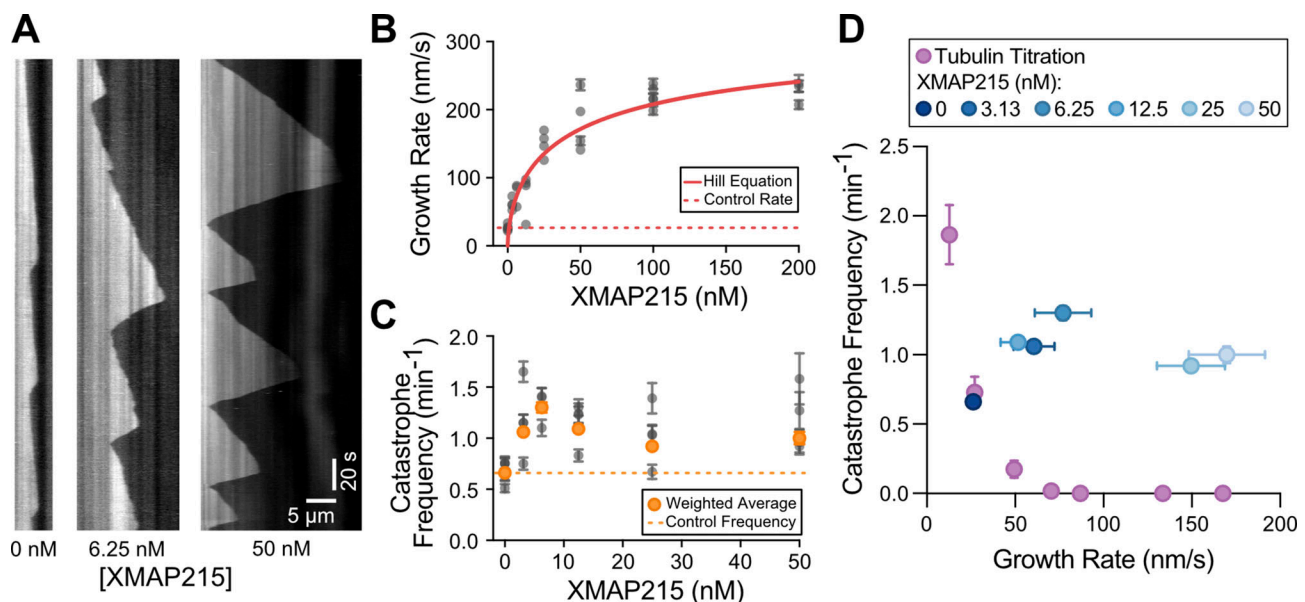


Figure 1. **XMAP215 simultaneously increases microtubule growth rate and catastrophe frequency in the presence of EB1.** (A) Representative kymographs of microtubule plus ends grown with 20 μM tubulin, 200 nM EB1-GFP, and corresponding amount of XMAP215 (nM). Tubulin signal is shown. (B and C) Quantification of microtubule growth rate (B) and catastrophe frequency (C) as a function of XMAP215 concentration in the presence of 20 μM tubulin and 200 nM EB1-GFP. Error bars, SEM and SE, respectively. Each point represents 20 kymographs from one experimental repeat. Number of experimental repeats per concentration, 6, 4, 3, 4, 4, and 3. Dotted lines indicate the average control values (0 nM XMAP215). Solid red line in B, fit to the Hill equation. Orange points in C, weighted averages for each condition. (D) Average catastrophe frequency (from C) replotted as a function of average growth rate (from B) for the XMAP215 titration along with the tubulin titration (Fig. S1 B).

establish an inverse correlation between GTP-cap size and catastrophe frequency when increase in growth rate is achieved by increasing tubulin concentration in the presence of EB1 (Fig. S1 D). This finding is consistent with a model in which faster microtubule growth leads to a larger GTP-cap, which in turn provides enhanced protection against catastrophe.

Increasing the microtubule growth rate using XMAP215 results in a simultaneous increase in catastrophe frequency

In cells, fast microtubule growth rates are achieved through the action of polymerases and other MAPs, including XMAP215 and EB1 (Akhmanova and Steinmetz, 2015). Interestingly, previous *in vitro* studies with XMAP215, either alone or in combination with EB1, reported that XMAP215-mediated increase in growth rate was not accompanied by a suppression of catastrophe frequency (Zanic et al., 2013; Vasquez et al., 1994). To investigate the relationship between catastrophe frequency and growth rate in the presence of XMAP215, we quantified microtubule dynamics over a range of XMAP215 concentrations (3.13–200 nM) in the background of 20 μ M tubulin and 200 nM EB1-GFP (Fig. 1 A). As expected, growth rate increased as a function of XMAP215 concentration (Fig. 1 B). The increase in growth rate was accompanied by more frequent catastrophe events, even with the lowest XMAP215 concentration used (Fig. 1 C). This relationship between growth rate and catastrophe frequency in the presence of XMAP215 is in stark contrast to that observed when growth rates were increased using tubulin titration (Fig. 1 D). Notably, XMAP215 led to a simultaneous increase in both growth rate and catastrophe frequency even in the absence of EB1 (Fig. S2), demonstrating that the observed increase in catastrophe frequency can be directly attributed to XMAP215.

Promotion of catastrophe by XMAP215 is not achieved through a reduction in the GTP-cap size

One possible explanation for the observed increase in catastrophe frequency is that XMAP215 may be directly reducing the

size of the protective GTP-cap. While a linear increase in GTP-cap size with microtubule growth rate is well established for tubulin titration (Fig. S1 C; Bieling et al., 2007; Strothman et al., 2019), whether the GTP-cap size increases with XMAP215 is not known. Our measurements of EB1 comets with XMAP215 titration revealed a direct correlation between growth rate and EB1 comet length (Fig. 2 A). This finding suggests that increasing growth rate by XMAP215 also results in a larger GTP-cap size, similar to what was observed when the growth rate was increased using higher tubulin concentrations (Fig. S1 C).

To directly compare the mean GTP-cap size in the presence or absence of XMAP215, we next performed growth rate-matching experiments. We found that growth rates achieved with 60 μ M tubulin and 200 nM EB1-GFP (condition I) could be matched using 20 μ M tubulin, 200 nM EB1-GFP, and 25 nM XMAP215 (condition II; Fig. 2 B). To precisely compare the EB1 comet sizes, we generated averaged EB1 comet intensity profiles for each of the two conditions (see Materials and methods; Bieling et al., 2007). Surprisingly, we found that the decay length of the EB1 comets was larger in the presence of XMAP215 (Fig. 2 C; 650 ± 20 nm, mean \pm 95% CI, versus 610 ± 20 nm in the absence of XMAP215), in spite of the significantly higher catastrophe frequency when compared with the tubulin control (0.30 ± 0.09 min⁻¹, standard error [SE], $n = 12$ catastrophes in 39 min of growth over 20 kymographs, versus 0.00 ± 0.03 min⁻¹, $n = 0$ catastrophes in 40 min of growth over 20 kymographs). This finding directly demonstrates that promotion of catastrophe by XMAP215 is not a result of a decrease in the mean GTP-cap size.

XMAP215 increases growth rate fluctuations and induces tapered microtubule ends

Our growth rate-matching experiments provided an excellent dataset for a direct comparison of microtubule growth characteristics in the presence and absence of XMAP215. While the mean growth rates were matched, we wondered whether the

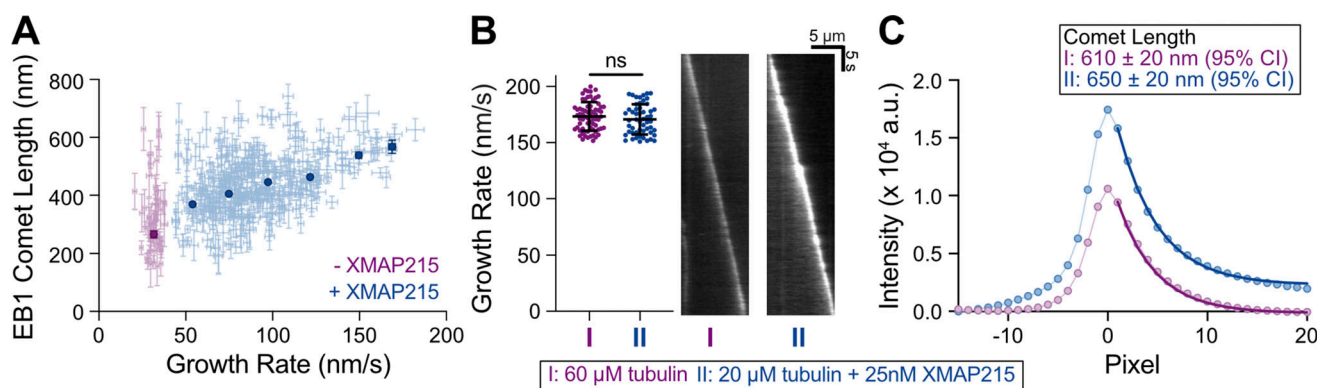


Figure 2. **XMAP215 does not decrease the GTP-cap size.** (A) Mean EB1 comet length as a function of microtubule growth rate over a range of XMAP215 concentrations (0–50 nM) in the presence of 20 μ M tubulin and 200 nM EB1-GFP. Dim points represent individual 30-s growth segments. Error bars, 95% CI. Bold points are weighted means; error bars, weighted error. For -XMAP215 condition (0 nM XMAP215), all individual segments from a single experiment were averaged. For +XMAP215 condition (3.13–50 nM XMAP215), individual segments were binned using growth rate into 25-nm/s bins and averaged. 20 microtubule kymographs were analyzed from each condition. A total of six experimental conditions were performed over 2 d. (B) Microtubules were polymerized with either 60 μ M tubulin and 200 nM EB1-GFP (condition I) or 20 μ M tubulin, 200 nM EB1-GFP, and 25 nM XMAP215 (condition II) to obtain growth rate-matched conditions. Left: 69 growth segments for condition I and 53 growth segments for condition II, with no significant difference in growth rate ($P = 0.28$, unpaired *t* test), were analyzed. Means and SD are shown. Right: Representative kymographs of EB1 localization. (C) The super-averaged EB1 comet profiles were fitted to an exponential decay (dark lines) to determine the average comet lengths (see Materials and methods). Error, 95% CI of the fit.

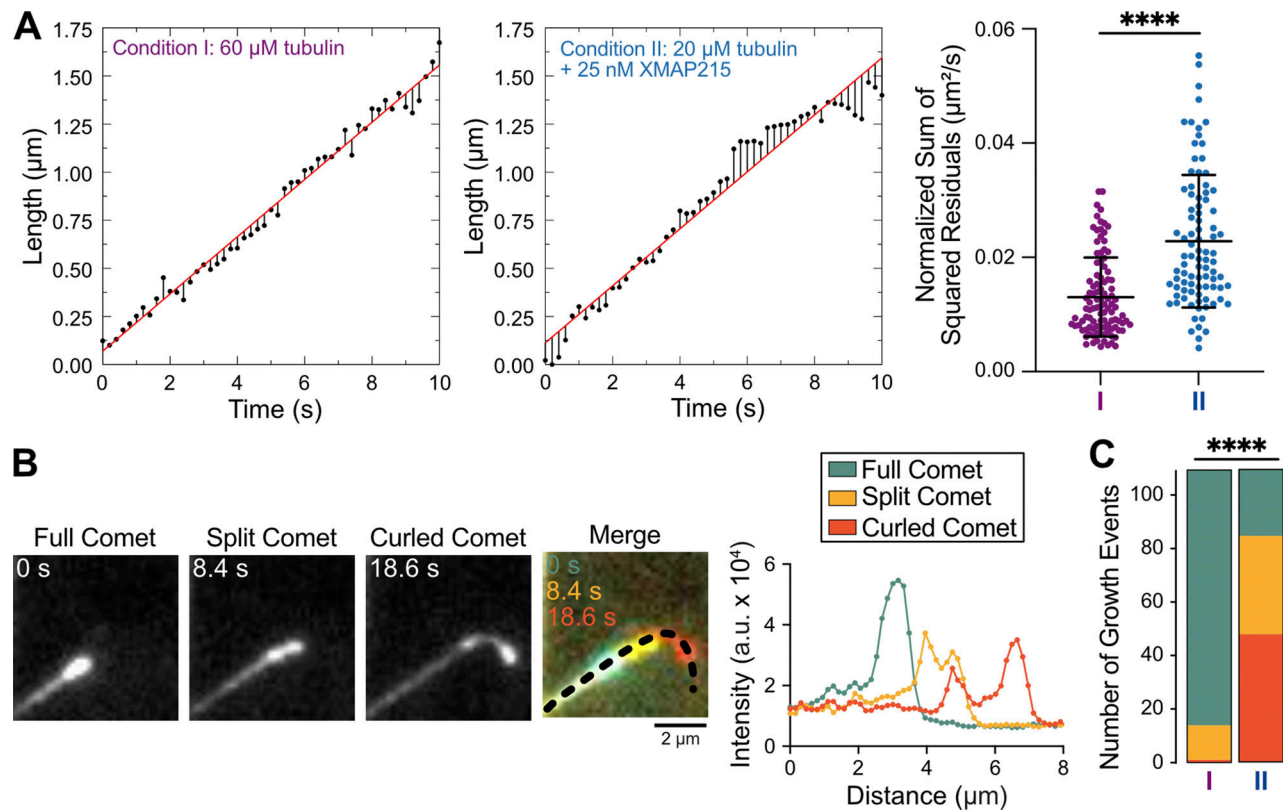


Figure 3. XMAP215 promotes microtubule growth rate fluctuations and tapered microtubule ends. Growth rate-matching conditions achieved by either 60 μM tubulin and 200 nM EB1-GFP (condition I) or 20 μM tubulin, 200 nM EB1-GFP, and 12.5/25 nM XMAP215 (condition II). **(A)** SSR was determined from 10-s segments that only displayed full comets. Left and center: Representative tracks showing microtubule tip position (black points), residuals for each time point (black lines), and linear regression to tip position (red line). Right: SSR for each segment; condition I, $0.013 \pm 0.007 \mu\text{m}^2/\text{s}$ (mean \pm SD, $n = 103$); condition II, $0.02 \pm 0.01 \mu\text{m}^2/\text{s}$ ($n = 90$). ****, $P < 0.0001$, unpaired Welch's t test. **(B)** An example microtubule with distinct EB1 comet morphologies: full, split, and curled. Intensity profiles along the dashed line at indicated time points. **(C)** Classification of 110 growth events into comet morphology categories. Condition I: 96 full, 13 split, 1 curled; condition II: 25 full, 37 split, 48 curled. ****, $P < 0.0001$, χ^2 test.

fluctuations in growth rate may differ between the two conditions. To investigate this possibility, we tracked microtubule growth and determined deviations from the mean growth rate using linear regression (Fig. 3 A). We found that the sum of squared residuals (SSR) was significantly higher in the presence of XMAP215 ($0.02 \pm 0.01 \mu\text{m}^2/\text{s}$, mean \pm SD, $n = 90$) than in the tubulin control conditions ($0.013 \pm 0.007 \mu\text{m}^2/\text{s}$, $n = 103$; $P < 0.0001$, unpaired Welch's t test; Fig. 3 A), despite no difference in the mean growth rate (Fig. S3 A). This result was further corroborated by mean squared displacement (MSD) analysis of the growing end positions in the presence and absence of XMAP215 (Fig. S3 B). Thus, we conclude that microtubules polymerizing with XMAP215 display a higher degree of growth rate variability than those polymerizing at the same growth rates in the absence of XMAP215.

Interestingly, our high-spatiotemporal-resolution tracking of EB1-GFP localization at microtubule ends polymerized with XMAP215 also revealed a range of comet morphologies evolving over time (Video 1 and Fig. 3 B). Canonical EB localization is a single peak of fluorescence that exponentially decays along the microtubule lattice (Bieling et al., 2007), hereafter referred to as a full comet (Fig. 3 B). However, in the presence of XMAP215, we observed frequent incidences of EB1 comets that appeared to split into two distinct intensity peaks, displaying a leading and a

lagging comet, both growing in the original growth direction (Fig. 3 B). After comet splitting, we occasionally observed the lagging comet catching up to the leading comet, a phenomenon previously termed a tip repair event (Aher et al., 2018; Doodhi et al., 2016). Furthermore, we observed that a large number of split comets led to a curled comet morphology, growing away from the original direction and resulting in polymer bending (Fig. 3 B). Quantification of the comet morphologies revealed that microtubules polymerized with XMAP215 were six times more likely to display a tapered end (either split or curled comet) when compared with those grown at the same growth rate without XMAP215 (Fig. 3 C; increase from 14 in the absence to 85 in the presence of XMAP215, out of 110 comets quantified for each condition, $P < 0.0001$, χ^2 test). Given that the growth rates were the same between the control and XMAP215 conditions, these observations suggest that the increase in the frequency of tapered microtubule ends is a direct consequence of XMAP215.

At the moment of catastrophe, microtubules grown with XMAP215 exhibit faster growth rates and higher EB1 localization

Our results suggested that XMAP215 disrupts the structural integrity of the GTP-cap by inducing fluctuations in growth and

promoting tapered microtubule ends. We hypothesized that these disruptions make microtubules more prone to catastrophe. To gain insight into the process of GTP-cap loss leading to catastrophe, we compared microtubule end position and EB1 intensity during catastrophe events using 0 and 3.13 nM XMAP215 conditions (in the background of 20 μ M tubulin and 200 nM EB1-GFP), which both displayed robust, but distinct, catastrophe frequencies (0 nM XMAP215, $0.76 \pm 0.06 \text{ min}^{-1}$, SE, $n = 161$ catastrophes over 213 min in growth; 3.13 nM XMAP215, $1.15 \pm 0.08 \text{ min}^{-1}$, $n = 205$ catastrophes over 178 min in growth). Microtubules polymerized in the absence of XMAP215 experienced a slowdown in growth rate over several seconds before the onset of catastrophe, accompanied by a decrease in EB1 intensity at microtubule ends (Fig. 4 A), as previously reported (Maurer et al., 2012; Maurer et al., 2014). In contrast, the transition to catastrophe was more abrupt in the presence of XMAP215. The instantaneous growth rate at the moment of catastrophe (measured over a 1-s time window) was significantly higher for microtubules polymerized with XMAP215 (Fig. 4 B; 0 nM XMAP215, $4 \pm 30 \text{ nm/s}$, mean \pm SD, $n = 27$; 3.13 nM XMAP215, $44 \pm 50 \text{ nm/s}$, $n = 27$, $P < 0.001$, unpaired Welch's t test), indicating that the transition to catastrophe in the presence of XMAP215 does not require a slowdown in growth to the level observed for microtubules grown without XMAP215. Furthermore, the residual intensity of EB1 measured at the highest-intensity pixel at the moment of catastrophe was significantly larger for microtubules grown with XMAP215 (Fig. 4 C; 0 nM XMAP215, $9,000 \pm 2,000 \text{ a.u.}$, mean \pm SD, $n = 27$; 3.13 nM XMAP215, $12,000 \pm 4,000 \text{ a.u.}$, $n = 27$, $P = 0.003$, unpaired Welch's t test), suggesting that an even larger GTP-cap density is not sufficient to protect against catastrophe in the presence of XMAP215. Overall, our results demonstrate that microtubule ends grown with XMAP215 are inherently less stable, as they undergo catastrophe at faster growth rates and with more EB1, when compared with microtubules polymerized without XMAP215.

Conclusions

A cap of GTP-tubulin at the end of a growing microtubule is widely accepted as the determinant of microtubule stability (Mitchison and Kirschner, 1984; Drechsel and Kirschner, 1994; Desai and Mitchison, 1997; Duellberg et al., 2016; Roostalu et al., 2020). The size of the GTP-cap is defined by the balance between the rates of addition of new GTP-tubulin dimers to the growing end and hydrolysis of GTP to GDP within the polymer. On its own, an increase in growth rate is expected to increase the size of the GTP-cap, and thus confer enhanced stability to the growing microtubule. Indeed, our results using tubulin titration confirm that an increase in growth rate is accompanied by an increase in EB1 comet size, as well as a suppression of catastrophe (Fig. 5, A and B). However, these findings raise the puzzling question of how simultaneously fast yet highly dynamic microtubule growth, as observed in cells, can be achieved. One possible way to limit the size of the GTP-cap, and thus presumably facilitate catastrophe, is through acceleration of the GTP-hydrolysis rate. This mechanism has been proposed for EB proteins, which promote catastrophe even while inducing a

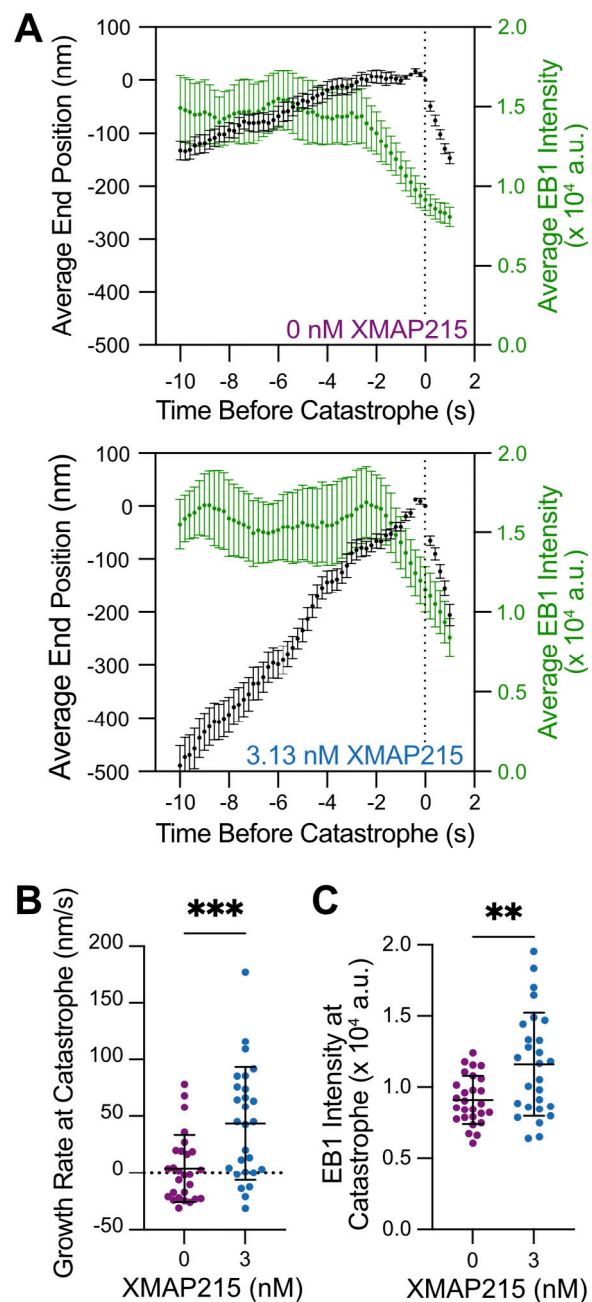


Figure 4. **Microtubules grown in the presence of XMAP215 undergo catastrophe at faster growth rates and with more EB1.** (A) Average microtubule end position and EB1 intensity over time. 27 events were averaged along their lifetime for both 0 and 3.13 nM XMAP215 conditions. Average EB1 intensity determined using a 1-s sliding window. Error bars, SEM. (B) Microtubule growth rate at the time of catastrophe determined for each growth event within a 1-s window before catastrophe. 0 nM XMAP215, $4 \pm 30 \text{ nm/s}$ (mean \pm SD, $n = 27$); 3.13 nM XMAP215, $44 \pm 50 \text{ nm/s}$ ($n = 27$). ***, $P < 0.001$, unpaired Welch's t test. (C) EB1 intensity at the time of catastrophe. 0 nM XMAP215, $9,000 \pm 2,000 \text{ a.u.}$ (SD, $n = 27$); 3.13 nM XMAP215, $12,000 \pm 4,000 \text{ a.u.}$ (SD, $n = 27$). **, $P = 0.003$ unpaired Welch's t test.

slight increase in growth rate (Bieling et al., 2007; Zhang et al., 2015; Vitre et al., 2008). Indeed, increasing EB concentration was reported to reduce the overall length of the EB comets in a dose-dependent manner (Maurer et al., 2011). In contrast, we

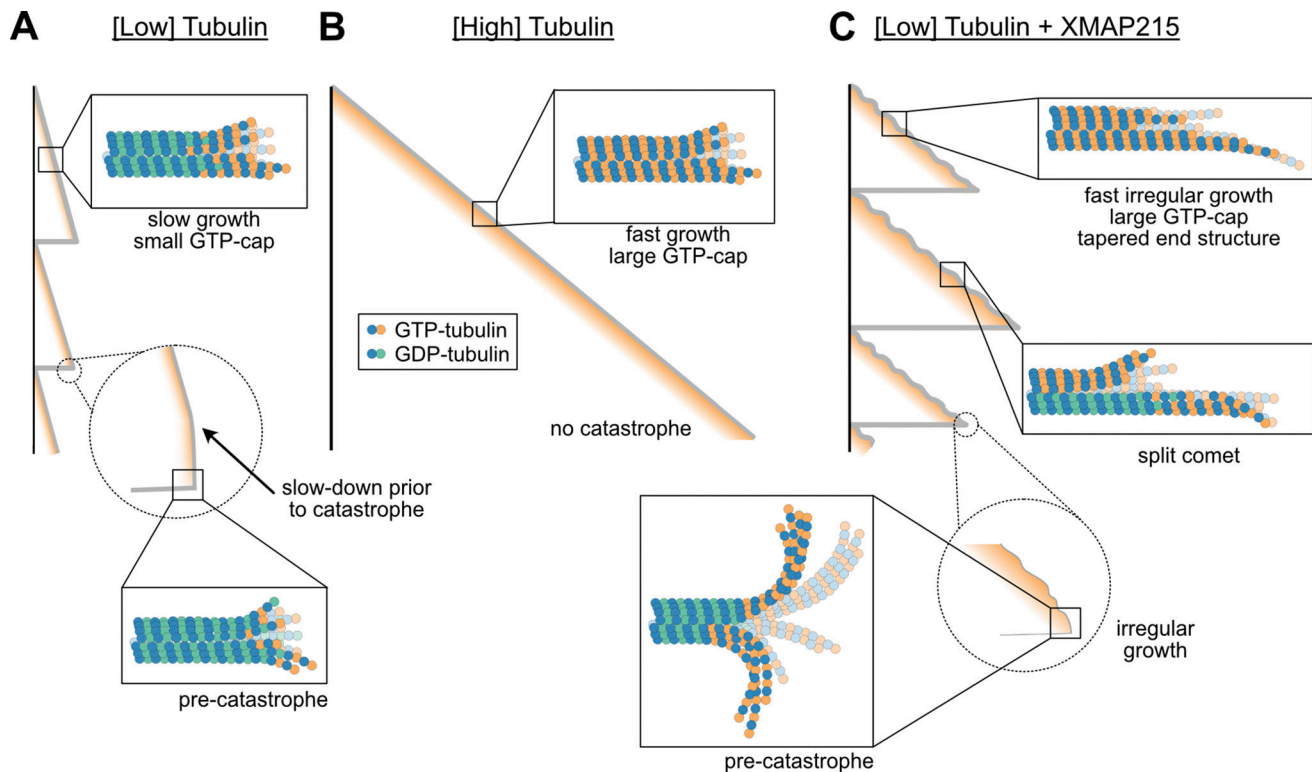


Figure 5. **XMAP215 drives microtubule catastrophe by perturbing the growing microtubule end structure.** (A) Microtubules polymerized with low tubulin grow slowly with small GTP-caps. Loss of GTP-tubulin triggers catastrophe. (B) Microtubules polymerized with high tubulin grow fast with large GTP-caps, resisting catastrophe. (C) Microtubules grown with XMAP215 display growth irregularities that trigger catastrophe, despite high GTP-tubulin content.

find that the mean length of the EB1 comets is increased when growth acceleration is achieved through the action of XMAP215. Thus, our results demonstrate that XMAP215 simultaneously promotes microtubule growth and catastrophe without accelerating the GTP-hydrolysis rate or otherwise decreasing the mean GTP-cap size.

In addition to its nucleotide composition, the structural configuration of the microtubule end is likely to play an important role in microtubule stability. Catastrophe is a complex phenomenon that does not follow first-order kinetics; rather, the probability of catastrophe increases with time spent in growth (Odde et al., 1995; Gardner et al., 2013; Gardner et al., 2011b). While the exact mechanisms of this aging process are still unknown, existing models typically associate specific structural configurations with the onset of catastrophe. These may involve accumulation of permanent defects including the uncapping and/or loss of individual protofilaments (Gardner et al., 2011b; Bowne-Anderson et al., 2013), gradual tapering of microtubule ends (Coombes et al., 2013), or dynamic evolution of stochastic end configurations involving protofilament curling (Zakharov et al., 2015). Notably, a variety of growing-end configurations have been observed by structural studies (McIntosh et al., 2018; Gudimchuk et al., 2020; Chrétien et al., 1995; Guesdon et al., 2016; Atherton et al., 2018; Mandelkow et al., 1991; Reid et al., 2019), and it has been previously proposed that some of these end configurations may indeed be energetically unfavorable, leading to catastrophe (Chrétien and Fuller, 2000; Hunyadi et al., 2005). Microtubule end structures can vary with tubulin

from different species (Orbach and Howard, 2019) and can be further modulated by MAPs and drugs (Chen and Hancock, 2015; Chen et al., 2019; Aher et al., 2018; Doodhi et al., 2016; Best et al., 2019; Arnal et al., 2000). In the case of XMAP215, our observations of EB1 comet splitting and end curling demonstrate that XMAP215 perturbs the structure of the growing microtubule end.

The canonical function of XMAP215 as a microtubule polymerase relies on its ability to bind curved tubulin conformation and stabilize an intermediate state in microtubule assembly (Brouhard et al., 2008; Ayaz et al., 2012; Brouhard and Rice, 2014). Given that XMAP215 was reported to act as a processive polymerase, with each XMAP215 molecule promoting the addition of ~25 tubulin dimers (Brouhard et al., 2008), we speculate that XMAP215 molecules primarily drive elongation of individual protofilaments, resulting in less coordinated protofilament growth. Indeed, our observations of EB1 comet splitting and curling suggest that polymerization is not synchronized among all protofilaments. Instead, XMAP215 promotes “sloppy” microtubule growth, with some protofilaments growing faster than others, to produce an overall tapered end (Fig. 5 C). Given that EBs localize to the interface of four tubulin dimers (Maurer et al., 2012), our observation of leading comets suggests the presence of multiple laterally connected protofilaments within these protrusions. The existence of tapered and open ends can further facilitate EB1 targeting (Reid et al., 2019), consistent with our observations of brighter EB1 comets in the presence of XMAP215 in growth rate-matching experiments. Importantly,

although we used EB1 to visualize the nucleotide composition of growing ends, our observation of XMAP215-dependent promotion of catastrophe in the absence of EB1 demonstrates that XMAP215 on its own, rather than through enhanced targeting of EB1, promotes catastrophe.

Uncoordinated assembly of individual protofilaments in the presence of XMAP215 may be manifested by increased fluctuations in growth (Kerssemakers et al., 2006; Howard and Hyman, 2009). Our results show that XMAP215 promotes large fluctuations in microtubule length over time even when ends display full comets. We speculate that the sloppy microtubule growth induced by XMAP215 is associated with a highly variable end structure, ultimately resulting in more frequent excursions into inherently unstable configurations, despite the presence of a large nucleotide cap (Fig. 5 C). Indeed, we find that both the instantaneous growth rate and the EB1 intensity at the moment of catastrophe are significantly higher for ends polymerized with XMAP215. Our results thus imply that there is no universal GTP-cap size threshold needed for the switch to catastrophe (Duellberg et al., 2016), and rather suggest that structural changes induced by XMAP215 can override the protective effects of the nucleotide cap.

Finally, while the polymerase effects of XMAP215 are dose dependent, such that the maximum growth promotion is reached in the ~100-nM range, we find that XMAP215's promotion of catastrophe reaches its full effect even at the lowest concentrations of XMAP215 tested. This observation provides further evidence of the distinct mechanisms regulating the absolute microtubule growth rate and overall microtubule stability. Future structural studies, combined with direct single-molecule measurements of microtubule assembly (Mickolajczyk et al., 2019), and the refinement of existing computational models (Bowne-Anderson et al., 2013; VanBuren et al., 2002; VanBuren et al., 2005; Margolin et al., 2012; Castle and Odde, 2013; Zakharov et al., 2015; Bollinger and Stevens, 2018; Igaev and Grubmüller, 2018; Kim and Rice, 2019; Michaels et al., 2020; Gudimchuk et al., 2020) will be necessary to unravel the full complexity of microtubule dynamics. Nevertheless, the ability to independently control the rates of growth and catastrophe is at the very core of microtubule regulation in cells, enabling the complex, dynamic remodeling of the microtubule cytoskeleton.

Materials and methods

Protein preparation

Bovine brain tubulin was purified as previously described through cycles of polymerization and depolymerization in a high-molarity Pipes buffer (Castoldi and Popov, 2003). Tubulin was labeled with either tetramethylrhodamine (TAMRA; Sigma-Aldrich) or Alexa Fluor 647 (Invitrogen) as previously described (Hyman et al., 1991). For imaging purposes, labeled tubulin was used at a ratio of 10% of the final tubulin concentration. XMAP215-7his expression construct was a kind gift from G. Brouhard (McGill University, Montreal, Canada). XMAP215 was expressed in Sf9 cells using the Bac-to-Bac system (Invitrogen) and purified using a HisTrap followed by gel filtration (adapted from Brouhard et al. [2008]), and stored in 10 mM Bis-Tris,

10 mM Tris HCl, 100 mM KCl, 1 mM DTT, and 10% glycerol, pH 6.6. EB1-GFP was expressed in *Escherichia coli*, purified as previously described (Zanic et al., 2009), and stored in 10 mM Bis-Tris, 10 mM Tris HCl, 100 mM KCl, 1 mM DTT, and 5% glycerol, pH 6.6. Protein concentration was determined using absorbance at $\lambda = 280$ nm.

Assay conditions and imaging

Samples were imaged in chambers constructed as previously described (Gell et al., 2010; Strothman et al., 2019). In brief, three strips of Parafilm were sandwiched between 22 × 22-mm and 18 × 18-mm silanized coverslips to create two narrow channels for the exchange of reaction solution. The channel surface was treated with 0.02 $\mu\text{g}/\mu\text{l}$ anti-TAMRA antibody (Invitrogen) followed by 1% Pluronic F127 (Sigma-Aldrich) before use. GMPCPP-stabilized, 25% TAMRA-labeled microtubules were polymerized as previously described (Hunter et al., 2003) and immobilized to coverslips using anti-TAMRA antibody (Gell et al., 2010). Imaging was performed using a Nikon Eclipse Ti microscope with a 100X/1.49-NA TIRF objective; Andor iXon Ultra electron-multiplying charge-coupled device camera; 488-, 561-, and 640-nm solid-state lasers (Nikon Lu-NA); Finger Lakes Instruments HS-625 high-speed emission filter wheel; and standard filter sets. A Tokai Hit objective heater was used to maintain the sample at 35°C. Images were acquired using NIS-Elements (Nikon). Acquisition rates were 0.6 frames per second for tubulin titration (Figs. 1 D and S1) and 5 frames per second otherwise.

The imaging buffer consisted of BRB80 supplemented with 40 mM D-glucose, 40 $\mu\text{g}/\text{ml}$ glucose oxidase, 25 $\mu\text{g}/\text{ml}$ catalase, 0.08 mg/ml casein, 10 mM DTT, and 0.1% methylcellulose. For tubulin titration (Figs. S1 and 1 D), reactions contained imaging buffer, concentrations of tubulin ranging from 12 to 60 μM , 200 nM EB1-GFP, 1 mM GTP, and 17 mM KCl. For XMAP215 titrations, reactions contained imaging buffer, 20 μM tubulin, concentrations of XMAP215 ranging from 3.13 to 200 nM, 1 mM GTP, and 200 nM EB1-GFP (Figs. 1, 2 A, and 4). For the XMAP215 titration without EB1 (Fig. S2), the reaction conditions were the same, except that EB1-GFP was not included. For growth rate-matched experiments (Fig. 2, B and C; Fig. 3; and Fig. S3), reactions contained imaging buffer, 200 nM EB1-GFP, 1 mM GTP, and concentrations of tubulin and XMAP215 as indicated in figure legends (condition I, 60 μM tubulin and no XMAP215; condition II, 20 μM tubulin and 12.5 or 25 nM XMAP215). In both XMAP215 titration and growth rate-matching experiments, XMAP215 storage buffer was consistently kept at a final concentration of 4× dilution (2.5 mM Bis-Tris, 2.5 mM Tris HCl, 25 mM KCl, 250 nM DTT, and 2.5% glycerol).

Microtubule dynamics analysis

Quantification of microtubule dynamics parameters was performed using microtubule kymographs generated in Fiji (Schindelin et al., 2012), as described previously (Zanic, 2016). For each experiment, 20 kymographs were generated using 5-pixel-wide lines in the tubulin channel and analyzed. In each kymograph, the faster-growing microtubule end was designated as the plus end; only plus-end dynamics were subsequently

analyzed. Catastrophe events were designated as a switch from growth to shrinkage that decreased microtubule length by more than 2 pixels (320 nm). Catastrophe frequency was calculated as the total number of catastrophe events divided by the total time spent in growth phase observed over 20 kymographs for an individual experiment, and SE was determined as the counting error (square root of the number of events divided by the total time spent in growth).

EB1 comet length analysis

EB1 comet lengths were determined using a series of custom Matlab (vR2020a; MathWorks) scripts. Briefly, beginnings and ends of individual growth events were manually determined on kymographs and divided into 30-s segments. For the analysis in Fig. 2 (B and C) only, 10-s segments (50 frames) were used to ensure highly accurate determination of segment velocities to be used in super-averaging into a single comet profile. The initial estimate of microtubule tip position over time was obtained assuming a constant growth rate. For each time frame, the pixel with the brightest EB1 intensity within a window (± 10 pixels, or ± 2 pixels for 12- μM condition in Fig. S1 C) around the initially estimated tip position was subsequently assigned as the microtubule tip position. The tip positions were then fitted by linear regression to assign a growth rate to each segment. Segments were then filtered to include only segments with well-defined growth rates using $R^2 > 0.9$ criterion, except for the 12- μM condition in Fig. S1 C, which displayed little displacement over a 30-s time period. To generate time-averaged intensity profiles, the determined tip positions from each temporal frame within the segment were aligned. The microtubule lattice intensity was determined by averaging the intensities of 5 pixels (located 5–10 pixels away from the tip for the 12- μM condition in Fig. S1 C, and 15–20 pixels away from the tip otherwise) and subsequently subtracted from the intensity of all pixels along the averaged intensity profile of a given segment. To compare comet lengths in growth rate-matching experiments in the absence and presence of XMAP215 (Fig. 2, B and C), 10-s segments with growth velocities of 150–200 nm/s were selected and further averaged to obtain a super-averaged intensity profile for each condition.

All growth segments used for the comet length measurements displayed full EB1 comet morphologies. To determine EB1 comet length, the averaged intensity profiles were fitted to an exponential decay function using 20 pixels starting with the pixel immediately following the tip position (Bieling et al., 2007):

$$Ae^{(-x/\lambda)},$$

where A is the intensity at pixel 1, and λ is the comet decay length. Exclusion of the 0th pixel intensity from the fit ensured that any potential subpixel perturbations in the tip structure not detected by our imaging did not affect the comet length measurement.

Determination of variability in microtubule growth

Individual microtubule growth events from the growth rate-matching conditions that displayed a full comet during their lifetime were subjected to automated tracking. Images were

background-subtracted using a rolling ball with a 5-pixel radius in Fiji. The EB1 channel was tracked with Fiesta's single-particle tracker (Ruhnnow et al., 2011) using Matlab. Then, a custom Matlab code was used to divide the output trajectories into continuous 10-s segments, allowing for gaps of no more than a total of 1 s within a given segment. The variations from the mean growth rate within the 10-s segments were quantified by performing residuals analysis as previously described (Lawrence et al., 2018). Briefly, using a custom Matlab code, a linear function was fitted to the length-versus-time data points to determine the mean growth rate. The SSR was calculated and normalized by the segment duration. For growth rate-matching experiments, only the trajectories with mean growth rates of 110–180 nm/s were considered. Outliers based on normalized SSR were identified using Matlab function "isoutlier" and subsequently discarded (12 outliers out of 115 tracks for 60 μM tubulin condition and 7 outliers out of 97 tracks for 20 μM tubulin + 12.5/25 nM XMAP215 condition). Unpaired t test with Welch's correction was used to determine P values for mean velocity and normalized SSR between experimental conditions. The same selected segments were subjected to MSD analysis using Matlab-based "msdanalyzer" (Tarantino et al., 2014). A quadratic function (Gardner et al., 2011a) was fitted to the first 5 s of the MSD curve:

$$MSD(t) = 2Dt + \nu^2 t^2 + \sigma^2,$$

where D is diffusion coefficient, ν is mean growth rate, and σ is positional error. The fit was weighted by the inverse of the SD of the MSD curve determined by msdanalyzer.

Determination of microtubule end morphology in growth rate-matching experiments

Microtubule end morphology was assessed from the EB1 channel for each experimental condition (condition I, 60 μM tubulin and 200 nM EB1-GFP; condition II, 20 μM tubulin, 200 nM EB1-GFP, and 12.5 or 25 nM XMAP215) using time-lapse videos and intensity profiles from kymographs produced from 7-pixel-wide (1,120 nm) lines. Individual microtubule growth events were tracked for ≤ 2 min, and the average microtubule growth rate was determined for each growth event. 110 growth events for each experimental condition, with no significant difference in growth rates between conditions, were scored for catastrophe and end morphology. End morphology was classified into three categories based on the EB1-GFP signal at the growing microtubule end: full, split, or curled comet. If EB1 localized in a single peak at the end of a growing microtubule for the entire duration, the event was classified as having a full comet. If two peaks in the intensity profile could be resolved (>2 pixels) for >1 s (5 frames), the comet was considered to be split. A curled comet was preceded by a splitting event, with the leading comet having grown outside the 7-pixel-wide linescan.

Determination of the growth rate and EB1 intensity at the onset of catastrophe

Our methods to determine the growth rate and the EB1-GFP intensity at the onset of catastrophe were developed based on previously published approaches (Maurer et al., 2012; Duellberg

et al., 2016). In brief, individual microtubule growth events from either 0 or 3.13 nM XMAP215 conditions that displayed only a full comet morphology over the 30 s before catastrophe were subjected to automated tracking. For each individual growth event, microtubule position was determined from the tubulin signal using TipTracker v3 (Prah et al., 2014). First, both x and y coordinates of the microtubule end from each temporal frame, except the initial and final frames, were preprocessed to eliminate tracking noise: if the difference between coordinates of the current frame and the previous frame was >1,000 nm, the current coordinate value was eliminated and a new coordinate value was interpolated using the previous and subsequent frame, assuming a linear growth rate (adapted from Rickman et al., 2017). To further minimize tracking noise, the “smoothdata” function in Matlab was used with the “movmedian” method and a 5-frame (1-s) window size. The end position was determined using smoothed coordinates. Initial determination of the time of catastrophe was performed manually and subsequently corrected using the following automated analysis. Each time point in the time interval of 10 frames before and after the manually approximated time of catastrophe was assigned an instantaneous growth rate using a linear fit over a 3-frame sliding window. Then, starting from 8 frames after catastrophe and moving backward in time, if 3 consecutive frames had velocity values greater than -50 nm/s, the latest of the three temporal frames was assigned as the time of catastrophe. After determining the time of catastrophe, the end-positions of growth events over time were aligned to generate an averaged microtubule tip position using a custom Matlab code. For each microtubule, time and position values were offset to assign the catastrophe event to (0,0). Subsequently, the mean and SEM for the positions at each time point were calculated for the two experimental conditions. The growth rate before catastrophe was determined using a custom Matlab function, performing a linear fit to the length-versus-time segments. To determine instantaneous growth rate at the time of catastrophe ($T = 0$ s), a 1-s (5-frame) window size (i.e., from $T = -1$ s to $T = 0$ s) was used.

EB1-GFP intensities at microtubule ends before catastrophe were determined using a custom Matlab function. Briefly, for each temporal frame, the EB1-GFP channel image was rotated, centering around the end position (determined using the tubulin signal, as described above), such that the microtubule was horizontally aligned. The brightest intensity value within 5 lattice pixels and 1 solution pixel was assigned as maximum EB1 intensity (5-pixel thickness, i.e., 5×6 -pixel² area). Local solution background intensity was determined by shifting the 5×6 -pixel² area up and down by 5 pixels, and the mean intensity was calculated. Temporal frames with <25 pixels available for background determination were discarded. For each temporal frame, the mean background intensity was then subtracted from the corresponding EB1 intensity. EB1 intensities along each event were determined by averaging the intensities within a 1-s (5-frame) sliding window immediately preceding the frame of interest. The intensities corresponding to the determined time of catastrophe ($T = 0$) were defined as EB1 intensity at catastrophe. Outliers in velocity and intensity were determined using isoutlier function in Matlab (3 outliers out of 30 events in 0-nM

XMAP215 condition; 1 outlier out of 28 events in 3.13-nM XMAP215 condition). The average EB1 intensities as a function of time were obtained by averaging all growth events at every time point, with error being the SEM, weighted by the inverse squared of the propagated SEM of the solution background within the 1-s window.

Online supplemental material

Fig. S1 shows that increasing the microtubule growth rate by increasing tubulin concentration correlates with larger EB1 comet lengths and suppression of microtubule catastrophe. Fig. S2 shows that XMAP215 alone promotes simultaneous increase of microtubule growth rate and catastrophe frequency. Fig. S3 shows matching growth rates used for the SSR analysis and also shows MSD analysis of growth rate fluctuations in the presence and absence of XMAP215. Video 1 shows EB1 comet morphologies at the end of a growing microtubule changing over time.

Acknowledgments

We thank G. Brouhard, W. Hancock, R. Ohi, the members of the Zanic laboratory, and the Vanderbilt Microtubules and Motors Club for discussions and feedback. XMAP215 construct was a kind gift from G. Brouhard (McGill University).

This work was supported by National Institutes of Health grant R35GM119552 to M. Zanic. V. Farmer acknowledges support from National Institutes of Health grant T32GM008320 and American Heart Association Predoctoral Fellowship 19PRE34380083. M. Zanic acknowledges support from the Human Frontier Science Program and the Searle Scholars Program.

The authors declare no competing financial interests.

Author contributions: M. Zanic, V. Farmer, and G. Arpağ conceptualized the project, designed the research, and wrote the manuscript. S. Hall and V. Farmer contributed reagents. V. Farmer performed experiments. G. Arpağ developed image analysis scripts. V. Farmer and G. Arpağ performed image and data analysis.

Submitted: 29 December 2020

Revised: 11 May 2021

Accepted: 8 July 2021

References

- Aher, A., M. Kok, A. Sharma, A. Rai, N. Olieric, R. Rodriguez-Garcia, E.A. Katrukha, T. Weinert, V. Olieric, L.C. Kapitein, et al. 2018. CLASP Suppresses Microtubule Catastrophes through a Single TOG Domain. *Dev. Cell.* 46:40–58.e8. <https://doi.org/10.1016/j.devcel.2018.05.032>
- Akhmanova, A., and M.O. Steinmetz. 2008. Tracking the ends: a dynamic protein network controls the fate of microtubule tips. *Nat. Rev. Mol. Cell Biol.* 9:309–322. <https://doi.org/10.1038/nrm2369>
- Akhmanova, A., and M.O. Steinmetz. 2015. Control of microtubule organization and dynamics: two ends in the limelight. *Nat. Rev. Mol. Cell Biol.* 16:711–726. <https://doi.org/10.1038/nrm4084>
- Al-Bassam, J., and F. Chang. 2011. Regulation of microtubule dynamics by TOG-domain proteins XMAP215/Dis1 and CLASP. *Trends Cell Biol.* 21: 604–614. <https://doi.org/10.1016/j.tcb.2011.06.007>
- Arnal, I., E. Karsenti, and A.A. Hyman. 2000. Structural transitions at microtubule ends correlate with their dynamic properties in *Xenopus* egg extracts. *J. Cell Biol.* 149:767–774. <https://doi.org/10.1083/jcb.149.4.767>

- Arpağ, G., E.J. Lawrence, V.J. Farmer, S.L. Hall, and M. Zanic. 2020. Collective effects of XMAP215, EB1, CLASP2, and MCAK lead to robust microtubule treadmilling. *Proc. Natl. Acad. Sci. USA*. 117:12847–12855. <https://doi.org/10.1073/pnas.2003191117>
- Atherton, J., M. Stouffer, F. Francis, and C.A. Moores. 2018. Microtubule architecture in vitro and in cells revealed by cryo-electron tomography. *Acta Crystallogr. D Struct. Biol.* 74:572–584. <https://doi.org/10.1107/S2059798318001948>
- Ayaz, P., X. Ye, P. Huddleston, C.A. Brautigam, and L.M. Rice. 2012. A TOG: α -tubulin Complex Structure Reveals Conformation-Based Mechanisms for a Microtubule Polymerase. *Science*. 337:857–860. <https://doi.org/10.1126/science.1221698>
- Best, R.L., N.E. LaPointe, J. Liang, K. Ruan, M.F. Shade, L. Wilson, and S.C. Feinstein. 2019. Tau isoform-specific stabilization of intermediate states during microtubule assembly and disassembly. *J. Biol. Chem.* 294:12265–12280. <https://doi.org/10.1074/jbc.RA119.009124>
- Bieling, P., L. Laan, H. Schek, E.L. Munteanu, L. Sandblad, M. Dogterom, D. Brunner, and T. Surrey. 2007. Reconstitution of a microtubule plus-end tracking system in vitro. *Nature*. 450:1100–1105. <https://doi.org/10.1038/nature06386>
- Bollinger, J.A., and M.J. Stevens. 2018. Catastrophic depolymerization of microtubules driven by subunit shape change. *Soft Matter*. 14:1748–1752. <https://doi.org/10.1039/C7SM02033C>
- Bowne-Anderson, H., M. Zanic, M. Kauer, and J. Howard. 2013. Microtubule dynamic instability: a new model with coupled GTP hydrolysis and multistep catastrophe. *BioEssays*. 35:452–461. <https://doi.org/10.1002/bies.201200131>
- Brouhard, G.J., and L.M. Rice. 2014. The contribution of α -tubulin curvature to microtubule dynamics. *J. Cell Biol.* 207:323–334. <https://doi.org/10.1083/jcb.201407095>
- Brouhard, G.J., J.H. Stear, T.L. Noetzel, J. Al-Bassam, K. Kinoshita, S.C. Harrison, J. Howard, and A.A. Hyman. 2008. XMAP215 is a processive microtubule polymerase. *Cell*. 132:79–88. <https://doi.org/10.1016/j.cell.2007.11.043>
- Castle, B.T., and D.J. Odde. 2013. Brownian dynamics of subunit addition-loss kinetics and thermodynamics in linear polymer self-assembly. *Biophys. J.* 105:2528–2540. <https://doi.org/10.1016/j.bpj.2013.10.009>
- Castoldi, M., and A.V. Popov. 2003. Purification of brain tubulin through two cycles of polymerization-depolymerization in a high-molarity buffer. *Protein Expr. Purif.* 32:83–88. [https://doi.org/10.1016/S1046-5928\(03\)00218-3](https://doi.org/10.1016/S1046-5928(03)00218-3)
- Chaaban, S., S. Jariwala, C.T. Hsu, S. Redemann, J.M. Kollman, T. Müller-Reichert, D. Sept, K.H. Bui, and G.J. Brouhard. 2018. The Structure and Dynamics of *C. elegans* Tubulin Reveals the Mechanistic Basis of Microtubule Growth. *Dev. Cell*. 47:191–204.e8. <https://doi.org/10.1016/j.devcel.2018.08.023>
- Chen, Y., and W.O. Hancock. 2015. Kinesin-5 is a microtubule polymerase. *Nat. Commun.* 6:8160. <https://doi.org/10.1038/ncomms9160>
- Chen, G.-Y., J.M. Cleary, A.B. Asenjo, Y. Chen, J.A. Mascaro, D.F.J. Argenteanu, H. Sosa, and W.O. Hancock. 2019. Kinesin-5 Promotes Microtubule Nucleation and Assembly by Stabilizing a Lattice-Competent Conformation of Tubulin. *Curr. Biol.* 29:2259–2269.e4. <https://doi.org/10.1016/j.cub.2019.05.075>
- Chrétien, D., and S.D. Fuller. 2000. Microtubules switch occasionally into unfavorable configurations during elongation. *J. Mol. Biol.* 298:663–676. <https://doi.org/10.1006/jmbi.2000.3696>
- Chrétien, D., S.D. Fuller, and E. Karsenti. 1995. Structure of growing microtubule ends: two-dimensional sheets close into tubes at variable rates. *J. Cell Biol.* 129:1311–1328. <https://doi.org/10.1083/jcb.129.5.1311>
- Coombs, C.E., A. Yamamoto, M.R. Kenzie, D.J. Odde, and M.K. Gardner. 2013. Evolving tip structures can explain age-dependent microtubule catastrophe. *Curr. Biol.* 23:1342–1348. <https://doi.org/10.1016/j.cub.2013.05.059>
- Desai, A., and T.J. Mitchison. 1997. Microtubule polymerization dynamics. *Annu. Rev. Cell Dev. Biol.* 13:83–117. <https://doi.org/10.1146/annurev.cellbio.13.1.83>
- Doodhi, H., A.E. Prota, R. Rodríguez-García, H. Xiao, D.W. Custer, K. Bargsen, E.A. Katrukha, M. Hilbert, S. Hua, K. Jiang, et al. 2016. Termination of Protofilament Elongation by Eribulin Induces Lattice Defects that Promote Microtubule Catastrophes. *Curr. Biol.* 26:1713–1721. <https://doi.org/10.1016/j.cub.2016.04.053>
- Drechsel, D.N., and M.W. Kirschner. 1994. The minimum GTP cap required to stabilize microtubules. *Curr. Biol.* 4:1053–1061. [https://doi.org/10.1016/S0960-9822\(00\)00243-8](https://doi.org/10.1016/S0960-9822(00)00243-8)
- Drechsel, D.N., A.A. Hyman, M.H. Cobb, and M.W. Kirschner. 1992. Modulation of the dynamic instability of tubulin assembly by the microtubule-associated protein tau. *Mol. Biol. Cell*. 3:1141–1154. <https://doi.org/10.1091/mbc.3.10.1141>
- Duellberg, C., N.I. Cade, D. Holmes, and T. Surrey. 2016. The size of the EB cap determines instantaneous microtubule stability. *eLife*. 5:e13470. <https://doi.org/10.7554/eLife.13470>
- Gard, D.L., and M.W. Kirschner. 1987. A microtubule-associated protein from *Xenopus* eggs that specifically promotes assembly at the plus-end. *J. Cell Biol.* 105:2203–2215. <https://doi.org/10.1083/jcb.105.5.2203>
- Gard, D.L., B.E. Becker, and S. Josh Romney. 2004. MAPping the eukaryotic tree of life: structure, function, and evolution of the MAP215/Dis1 family of microtubule-associated proteins. *Int. Rev. Cytol.* 239:179–272. [https://doi.org/10.1016/S0074-7696\(04\)39004-2](https://doi.org/10.1016/S0074-7696(04)39004-2)
- Gardner, M.K., B.D. Charlebois, I.M. Jánosi, J. Howard, A.J. Hunt, and D.J. Odde. 2011a. Rapid microtubule self-assembly kinetics. *Cell*. 146:582–592. <https://doi.org/10.1016/j.cell.2011.06.053>
- Gardner, M.K., M. Zanic, C. Gell, V. Bormuth, and J. Howard. 2011b. Depolymerizing kinesins Kip3 and MCAK shape cellular microtubule architecture by differential control of catastrophe. *Cell*. 147:1092–1103. <https://doi.org/10.1016/j.cell.2011.10.037>
- Gardner, M.K., M. Zanic, and J. Howard. 2013. Microtubule catastrophe and rescue. *Curr. Opin. Cell Biol.* 25:14–22. <https://doi.org/10.1016/j.ceb.2012.09.006>
- Gell, C., V. Bormuth, G.J. Brouhard, D.N. Cohen, S. Diez, C.T. Friel, J. Helenius, B. Nitzsche, H. Petzold, J. Ribbe, et al. 2010. Microtubule dynamics reconstituted in vitro and imaged by single-molecule fluorescence microscopy. *Methods Cell Biol.* 95:221–245.
- Gudimchuk, N.B., E.V. Ulyanov, E. O’Toole, C.L. Page, D.S. Vinogradov, G. Morgan, G. Li, J.K. Moore, E. Szczesna, A. Roll-Mecak, et al. 2020. Mechanisms of microtubule dynamics and force generation examined with computational modeling and electron cryotomography. *Nat. Commun.* 11:3765. <https://doi.org/10.1038/s41467-020-17553-2>
- Guesdon, A., F. Bazile, R.M. Buey, R. Mohan, S. Monier, R.R. García, M. Angevin, C. Heichette, R. Wieneke, R. Tampé, et al. 2016. EB1 interacts with outwardly curved and straight regions of the microtubule lattice. *Nat. Cell Biol.* 18:1102–1108. <https://doi.org/10.1038/ncb3412>
- Howard, J., and A.A. Hyman. 2009. Growth, fluctuation and switching at microtubule plus ends. *Nat. Rev. Mol. Cell Biol.* 10:569–574. <https://doi.org/10.1038/nrm2713>
- Hunter, A.W., M. Caplow, D.L. Coy, W.O. Hancock, S. Diez, L. Wordeman, and J. Howard. 2003. The kinesin-related protein MCAK is a microtubule depolymerase that forms an ATP-hydrolyzing complex at microtubule ends. *Mol. Cell*. 11:445–457. [https://doi.org/10.1016/S1097-2765\(03\)00049-2](https://doi.org/10.1016/S1097-2765(03)00049-2)
- Hunyadi, V., D. Chrétien, and I.M. Jánosi. 2005. Mechanical stress induced mechanism of microtubule catastrophes. *J. Mol. Biol.* 348:927–938. <https://doi.org/10.1016/j.jmb.2005.03.019>
- Hyman, A., D. Drechsel, D. Kellogg, S. Salser, K. Sawin, P. Steffen, L. Wordeman, and T. Mitchison. 1991. Preparation of modified tubulins. *Methods Enzymol.* 196:478–485. [https://doi.org/10.1016/0076-6879\(91\)96041-0](https://doi.org/10.1016/0076-6879(91)96041-0)
- Igaev, M., and H. Grubmüller. 2018. Microtubule assembly governed by tubulin allosteric gain in flexibility and lattice induced fit. *eLife*. 7:e34353. <https://doi.org/10.7554/eLife.34353>
- Kerssemakers, J.W.J., E.L. Munteanu, L. Laan, T.L. Noetzel, M.E. Janson, and M. Dogterom. 2006. Assembly dynamics of microtubules at molecular resolution. *Nature*. 442:709–712. <https://doi.org/10.1038/nature04928>
- Kim, T., and L.M. Rice. 2019. Long-range, through-lattice coupling improves predictions of microtubule catastrophe. *Mol. Biol. Cell*. 30:1451–1462. <https://doi.org/10.1091/mbc.E18-10-0641>
- Lawrence, E.J., G. Arpağ, S.R. Norris, and M. Zanic. 2018. Human CLASP2 specifically regulates microtubule catastrophe and rescue. *Mol. Biol. Cell*. 29:1168–1177. <https://doi.org/10.1091/mbc.E18-01-0016>
- Mandelkow, E.-M., E. Mandelkow, and R.A. Milligan. 1991. Microtubule dynamics and microtubule caps: a time-resolved cryo-electron microscopy study. *J. Cell Biol.* 114:977–991. <https://doi.org/10.1083/jcb.114.5.977>
- Margolin, G., I.V. Gregoret, T.M. Cickovski, C. Li, W. Shi, M.S. Alber, and H.V. Goodson. 2012. The mechanisms of microtubule catastrophe and rescue: implications from analysis of a dimer-scale computational model. *Mol. Biol. Cell*. 23:642–656. <https://doi.org/10.1091/mbc.E11-08-0688>
- Maurer, S.P., P. Bieling, J. Cope, A. Hoenger, and T. Surrey. 2011. GTPgammaS microtubules mimic the growing microtubule end structure recognized by end-binding proteins (EBs). *Proc. Natl. Acad. Sci. USA*. 108:3988–3993. <https://doi.org/10.1073/pnas.1014758108>
- Maurer, S.P., F.J. Fourniol, G. Bohner, C.A. Moores, and T. Surrey. 2012. EBs recognize a nucleotide-dependent structural cap at growing microtubule ends. *Cell*. 149:371–382. <https://doi.org/10.1016/j.cell.2012.02.049>

- Maurer, S.P., N.I. Cade, G. Bohner, N. Gustafsson, E. Boutant, and T. Surrey. 2014. EB1 accelerates two conformational transitions important for microtubule maturation and dynamics. *Curr. Biol.* 24:372–384. <https://doi.org/10.1016/j.cub.2013.12.042>
- McIntosh, J.R., E. O'Toole, G. Morgan, J. Austin, E. Ulyanov, F. Ataullakhanov, and N. Gudimchuk. 2018. Microtubules grow by the addition of bent guanosine triphosphate tubulin to the tips of curved protofilaments. *J. Cell Biol.* 217:2691–2708. <https://doi.org/10.1083/jcb.201802138>
- Michaels, T.C.T., S. Feng, H. Liang, and L. Mahadevan. 2020. Mechanics and kinetics of dynamic instability. *eLife.* 9:e54077. <https://doi.org/10.7554/eLife.54077>
- Mickolajczyk, K.J., E.A. Geyer, T. Kim, L.M. Rice, and W.O. Hancock. 2019. Direct observation of individual tubulin dimers binding to growing microtubules. *Proc. Natl. Acad. Sci. USA.* 116:7314–7322. <https://doi.org/10.1073/pnas.1815823116>
- Mimori-Kiyosue, Y., I. Grigoriev, G. Lansbergen, H. Sasaki, C. Matsui, F. Severin, N. Galjart, F. Grosveld, I. Vorobjev, S. Tsukita, and A. Akhmanova. 2005. CLASP1 and CLASP2 bind to EB1 and regulate microtubule plus-end dynamics at the cell cortex. *J. Cell Biol.* 168:141–153. <https://doi.org/10.1083/jcb.200405094>
- Mitchison, T., and M. Kirschner. 1984. Dynamic instability of microtubule growth. *Nature.* 312:237–242. <https://doi.org/10.1038/312237a0>
- O'Brien, E.T., E.D. Salmon, R.A. Walker, and H.P. Erickson. 1990. Effects of magnesium on the dynamic instability of individual microtubules. *Bichemistry.* 29:6648–6656. <https://doi.org/10.1021/bi00480a014>
- Odde, D.J., L. Cassimeris, and H.M. Buettner. 1995. Kinetics of microtubule catastrophe assessed by probabilistic analysis. *Biophys. J.* 69:796–802. [https://doi.org/10.1016/S0006-3495\(95\)79953-2](https://doi.org/10.1016/S0006-3495(95)79953-2)
- Orbach, R., and J. Howard. 2019. The dynamic and structural properties of axonemal tubulins support the high length stability of cilia. *Nat. Commun.* 10:1838. <https://doi.org/10.1038/s41467-019-09779-6>
- Piedra, F.-A., T. Kim, E.S. Garza, E.A. Geyer, A. Burns, X. Ye, and L.M. Rice. 2016. GDP-to-GTP exchange on the microtubule end can contribute to the frequency of catastrophe. *Mol. Biol. Cell.* 27:3515–3525. <https://doi.org/10.1091/mbc.e16-03-0199>
- Prahl, L.S., B.T. Castle, M.K. Gardner, and D.J. Odde. 2014. Quantitative analysis of microtubule self-assembly kinetics and tip structure. *Methods Enzymol.* 540:35–52.
- Reid, T.A., C. Coombes, S. Mukherjee, R.R. Goldblum, K. White, S. Parmar, M. McClellan, M. Zanic, N. Courtemanche, and M.K. Gardner. 2019. Structural state recognition facilitates tip tracking of EB1 at growing microtubule ends. *eLife.* 8:e48117. <https://doi.org/10.7554/eLife.48117>
- Rickman, J., C. Duellberg, N.I. Cade, L.D. Griffin, and T. Surrey. 2017. Steady-state EB cap size fluctuations are determined by stochastic microtubule growth and maturation. *Proc. Natl. Acad. Sci. USA.* 114:3427–3432. <https://doi.org/10.1073/pnas.1620274114>
- Roostalu, J., C. Thomas, N.I. Cade, S. Kunzelmann, I.A. Taylor, and T. Surrey. 2020. The speed of GTP hydrolysis determines GTP cap size and controls microtubule stability. *eLife.* 9:e51992. <https://doi.org/10.7554/eLife.51992>
- Ruhnow, F., D. Zwicker, and S. Diez. 2011. Tracking single particles and elongated filaments with nanometer precision. *Biophys. J.* 100:2820–2828. <https://doi.org/10.1016/j.bpj.2011.04.023>
- Rusan, N.M., C.J. Fagerstrom, A.-M.C. Yvon, and P. Wadsworth. 2001. Cell cycle-dependent changes in microtubule dynamics in living cells expressing green fluorescent protein-alpha tubulin. *Mol. Biol. Cell.* 12:971–980. <https://doi.org/10.1091/mbc.12.4.971>
- Schindelin, J., I. Arganda-Carreras, E. Frise, V. Kaynig, M. Longair, T. Pietzsch, S. Preibisch, C. Rueden, S. Saalfeld, B. Schmid, et al. 2012. Fiji: an open-source platform for biological-image analysis. *Nat. Methods.* 9:676–682. <https://doi.org/10.1038/nmeth.2019>
- Slep, K.C. 2009. The role of TOG domains in microtubule plus end dynamics. *Biochem. Soc. Trans.* 37:1002–1006. <https://doi.org/10.1042/BSTO371002>
- Strothman, C., V. Farmer, G. Arpağ, N. Rodgers, M. Podolski, S. Norris, R. Ohi, and M. Zanic. 2019. Microtubule minus-end stability is dictated by the tubulin off-rate. *J. Cell Biol.* 218:2841–2853. <https://doi.org/10.1083/jcb.201905019>
- Tarantino, N., J.Y. Tinevez, E.F. Crowell, B. Boisson, R. Henriques, M. Mhlanga, F. Agou, A. Israël, and E. Laplantine. 2014. TNF and IL-1 exhibit distinct ubiquitin requirements for inducing NEMO-IKK supra-molecular structures. *J. Cell Biol.* 204:231–245. <https://doi.org/10.1083/jcb.201307172>
- VanBuren, V., D.J. Odde, and L. Cassimeris. 2002. Estimates of lateral and longitudinal bond energies within the microtubule lattice. *Proc. Natl. Acad. Sci. USA.* 99:6035–6040. <https://doi.org/10.1073/pnas.092504999>
- VanBuren, V., L. Cassimeris, and D.J. Odde. 2005. Mechanochemical model of microtubule structure and self-assembly kinetics. *Biophys. J.* 89:2911–2926. <https://doi.org/10.1529/biophysj.105.060913>
- Vasquez, R.J., D.L. Gard, and L. Cassimeris. 1994. XMAP from *Xenopus* eggs promotes rapid plus end assembly of microtubules and rapid microtubule polymer turnover. *J. Cell Biol.* 127:985–993. <https://doi.org/10.1083/jcb.127.4.985>
- Vitre, B., F.M. Coquelle, C. Heichette, C. Garnier, D. Chrétien, and I. Arnal. 2008. EB1 regulates microtubule dynamics and tubulin sheet closure in vitro. *Nat. Cell Biol.* 10:415–421. <https://doi.org/10.1038/ncb1703>
- Walker, R.A., E.T. O'Brien, N.K. Pryer, M.F. Soboeiro, W.A. Voter, H.P. Erickson, and E.D. Salmon. 1988. Dynamic instability of individual microtubules analyzed by video light microscopy: rate constants and transition frequencies. *J. Cell Biol.* 107:1437–1448. <https://doi.org/10.1083/jcb.107.4.1437>
- Zakharov, P., N. Gudimchuk, V. Voevodin, A. Tikhonravov, F.I. Ataullakhanov, and E.L. Grishchuk. 2015. Molecular and Mechanical Causes of Microtubule Catastrophe and Aging. *Biophys. J.* 109:2574–2591. <https://doi.org/10.1016/j.bpj.2015.10.048>
- Zanic, M. 2016. Measuring the Effects of Microtubule-Associated Proteins on Microtubule Dynamics In Vitro. *Methods Mol. Biol.* 1413:47–61. https://doi.org/10.1007/978-1-4939-3542-0_4
- Zanic, M., J.H. Stear, A.A. Hyman, and J. Howard. 2009. EB1 recognizes the nucleotide state of tubulin in the microtubule lattice. *PLoS One.* 4:e7585. <https://doi.org/10.1371/journal.pone.0007585>
- Zanic, M., P.O. Widlund, A.A. Hyman, and J. Howard. 2013. Synergy between XMAP215 and EB1 increases microtubule growth rates to physiological levels. *Nat. Cell Biol.* 15:688–693. <https://doi.org/10.1038/ncb2744>
- Zhang, R., G.M. Alushin, A. Brown, and E. Nogales. 2015. Mechanistic origin of microtubule dynamic instability and its modulation by EB proteins. *Cell.* 162:849–859. <https://doi.org/10.1016/j.cell.2015.07.012>

Supplemental material

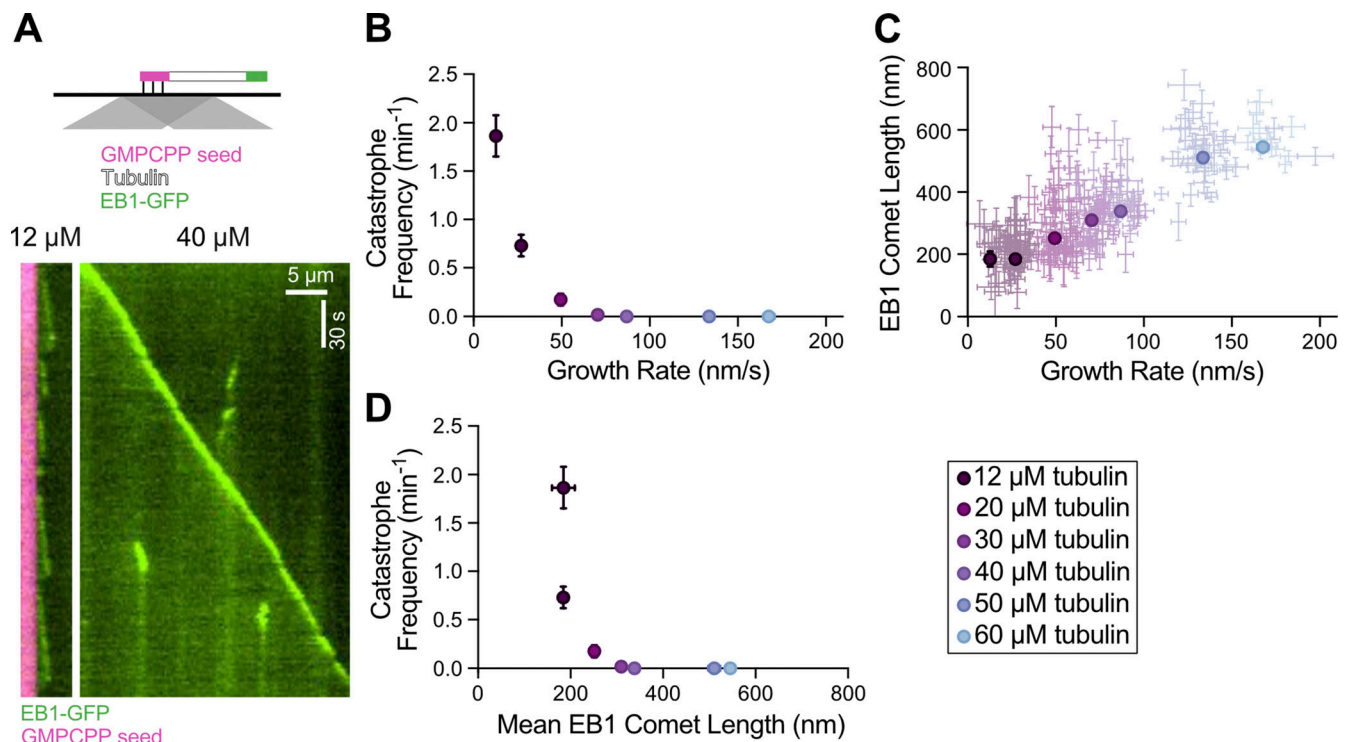


Figure S1. **Increasing the microtubule growth rate by increasing tubulin concentration correlates with larger EB1 comet lengths and suppression of microtubule catastrophe.** (A) Top: Schematic of TIRF assay. Dynamic microtubule extensions were polymerized from GMPCPP-stabilized seeds using unlabeled tubulin in the presence of EB1-GFP. Bottom: Representative kymographs of microtubule plus ends grown with either 12 or 40 μ M tubulin and 200 nM EB1-GFP. (B) Microtubule catastrophe frequency as a function of microtubule growth rate. Each point is the mean growth rate and catastrophe frequency for a single experimental condition. Error bars, SEM and SE, respectively. (C) EB1 comet length as a function of microtubule growth rate. Dim points are growth rates and comet lengths for individual 30-s growth segments. Error bars, 95% CI. Bold points are weighted means for each experimental condition, with error bars being the weighted error. (D) Catastrophe frequency (displayed in B) replotted as a function of mean EB1 comet length (displayed in C) for each experimental condition. For all panels, 20 microtubule kymographs were analyzed for each experimental condition. All experiments were performed on the same day.

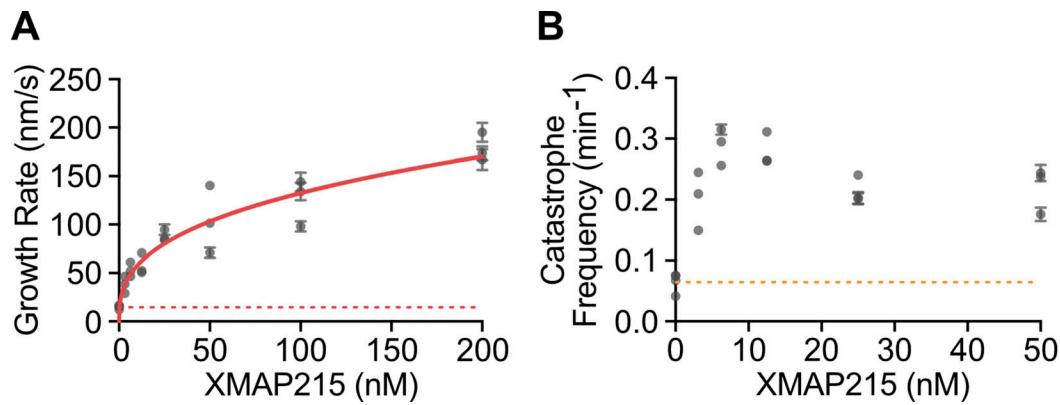


Figure S2. **XMAP215 alone promotes simultaneous increase of microtubule growth rate and catastrophe frequency.** (A and B) Quantification of microtubule growth rate (A) and catastrophe frequency (B) as a function of XMAP215 concentration in the presence of 10 μ M tubulin. Error bars, SEM and SE, respectively. Each point represents values measured for 20 kymographs from one experimental repeat. Number of experimental repeats per concentration, 4, 3, 3, 3, 3, 3. Dotted lines indicate the average values for the control (0 nM XMAP215). Solid red line in A is the data fit to the Hill equation.

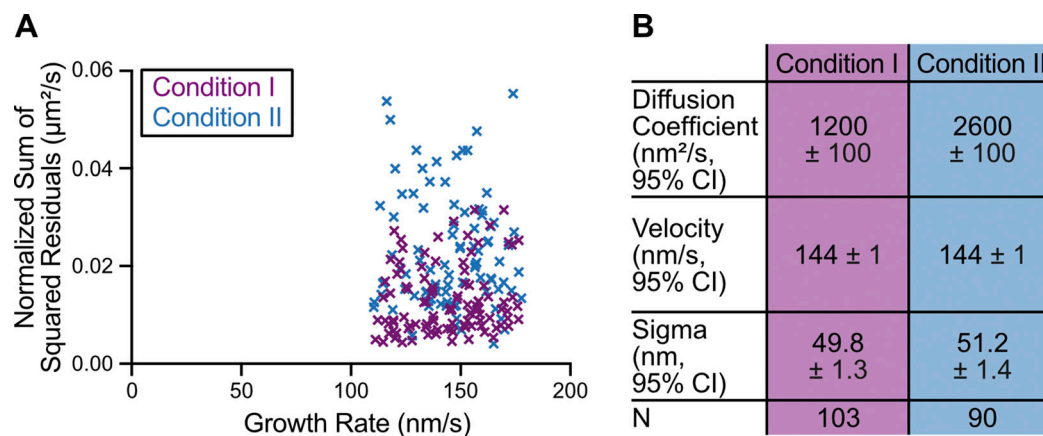


Figure S3. **Residual and MSD analyses indicate higher fluctuations in microtubule growth rate in the presence of XMAP215.** (A) Growth events used for SSR analysis in Fig. 3 A were selected to have no significant difference in growth rate: condition I (60 μ M tubulin and 200 nM EB1-GFP), 143 \pm 18 nm/s (mean \pm SD, $n = 103$); condition II (20 μ M tubulin, 200 nM EB1-GFP, and 12.5/25 nM XMAP215), 145 \pm 18 nm/s ($n = 90$). $P = 0.54$, t test. (B) MSD analysis was used to determine the diffusion coefficient (D), velocity (v), and positional error (σ) of microtubule growth by fitting a quadratic function, $\text{MSD}(t) = 2Dt^2 + vt^2 + \sigma^2$ (Gardner et al., 2011a).

Video 1. **EB1 comet morphologies at the end of a growing microtubule.** Time lapse of a microtubule grown in the presence of 20 μ M tubulin, 200 nM EB1-GFP, and 25 nM XMAP215. Scale bar, 2 μ m. Video play rate is 20 frames per second.